Journal of Materials Chemistry A

ROYAL SOCIETY OF CHEMISTRY

PAPER

View Article Online
View Journal | View Issue

Cite this: J. Mater. Chem. A, 2021, 9, 13044

Establishing structure/property relationships in atomically dispersed Co–Fe dual site M–N_x catalysts on microporous carbon for the oxygen reduction reaction†

Kai Wang, ‡[a] Jiapeng Liu, ‡[b] Zhenghua Tang, *[ac] Ligui Li, [a] Zheng Wang,[b] Muhammad Zubair, [d] Francesco Ciucci, *[be] Lars Thomsen,[f] Joshua Wright[g] and Nicholas M. Bedford *[d]

Received 8th April 2021
Accepted 10th May 2021

DOI: 10.1039/d1ta02925h

rsc.li/materials-a

Coupled metal–nitrogen–carbon (M–N_x–C) materials show great promise as platinum-group-metal (PGM) free catalysts for the oxygen reduction reaction (ORR). Herein, we report a facile strategy to construct atomically dispersed Co–Fe dual sites enriched on the surface of nitrogen doped microporous carbon (NC) as an efficient electrocatalyst for ORR. Synchrotron X-ray techniques indicate that the Co and Fe atoms are strongly correlated while further revealing that the longer-range lattice structure of NC is highly tunable. Density functional theory calculations reveal that the Co–Fe dimers are incorporated in the slightly disordered NC substrate, providing a lower adsorption free energy for O_2. The as-prepared CoFe–NC catalyst exhibited excellent ORR activities, while a CoFe–NC based zinc–air battery exhibited a power density of 115 mW cm^{-2} and a specific capacity of 791 mA h g^{-1}. This work showcases a straightforward methodology for creating atomically dispersed catalysts and illustrates the importance of understanding how dual metal sites impact electrocatalytic activity.

Introduction

To mitigate the global energy reliance on fossil fuels and to help alleviate worldwide environmental pollution issues, it is imperative to develop renewable and sustainable energy devices such as proton exchange membrane fuel cells (PEMFCs) and metal air batteries.[1,2] The oxygen reduction reaction (ORR) is a key process which significantly influences the energy conversion efficiency of the aforementioned devices, but is impeded partially by the reduction of strong O=O bonds (498 kJ mol^{-1}), resulting in sluggish reaction kinetics that necessitate electrocatalytic materials.[3] Platinum-based catalysts, especially Pt/C, have been the benchmark catalysts for desirable ORR reactivity, yet are commercially prohibited by the high cost and scarcity of Pt.[4] Additionally, Pt-based catalysts suffer from other ineluctable problems, such as poor durability for prolonged operation, susceptibility to methanol crossover and so on.[5,6]

In an effort to move away from Pt and similarly problematic Pt group metal (PGM) catalysts, first-row transition metal nitrogen-doped porous carbon (M–N_x–C) materials have gained serious attention as promising alternatives for ORR. Previous reports have demonstrated that M–N_x–C catalysts show excellent catalytic performances, which are coupled with their inherently low cost and potential ability to tune the chemistry/structure of the well-defined active sites, which has led to a surge in research activities.[7–9] In regards to ORR, the bonding energies of M–N_x sites with oxygen molecules and oxygenated intermediates are dependent on the nature of the transition metal and the local structure, which result in significantly different activities and stabilities.[10] With the high utilization of the metal centers and strong anchoring interactions between the nitrogen and metal atoms, atomically dispersed M–N_x–C catalysts (also often called single-atom catalysts, SACs) have

[a]Guangzhou Key Laboratory for Surface Chemistry of Energy Materials, New Energy Research Institute, School of Environment and Energy, South China University of Technology Guangzhou Higher Education Mega Center, Guangzhou, Guangdong, 510006, China. E-mail: zhht@scut.edu.cn

[b]Department of Mechanical and Aerospace Engineering, The Hong Kong University of Science and Technology, Hong Kong, SAR, 999077, China. E-mail: francesco.ciucci@ust.hk

[c]Key Laboratory of Fuel Cell Technology of Guangdong Province, School of Chemistry and Chemical Engineering, South China University of Technology, Guangzhou, 510640, China

[d]School of Chemical Engineering University of New South Wales Sydney, New South Wales, 2052, Australia

[e]Department of Chemical and Biological Engineering, The Hong Kong University of Science and Technology, Hong Kong, SAR, 999077, China

[f]Australian Synchrotron, ANSTO, Clayton, Victoria, 3168, Australia

[g]Department of Physics, Illinois Institute of Technology, Chicago, Illinois, 60616, USA. E-mail: n.bedford@unsw.edu.au

† Electronic supplementary information (ESI) available. See DOI: 10.1039/d1ta02925h

‡ These authors contributed equally to this work.

demonstrated excellent activities and robust stabilities, which are even superior to those of the state-of-the-art Pt/C catalyst for ORR.[11,12] For example, Wan *et al.* fabricated a concave-shaped Fe–N–C single atom catalyst with enhanced external surface area and dense Fe–N_4 moieties, which demonstrated an extremely high PEMFC activity that surpassed the 2018 US DOE targets.[13] Other atomically dispersed transition metal based M–N_x–C catalysts including Co–N_x–C,[14] Mn–N_x–C,[15] Ni–N_x–C,[16] Zn–N_x–C,[17] Cu–N_x–C,[18] Ir–N_x–C,[19] Cr–N_x–C,[20] and Ru–N_x–C[21] have also been explored for ORR electrocatalysis. The use of dual transition metal active sites in M–N_x–C has been increasingly studied as well, mainly due to the synergistic effects between the two metallic atoms that result in charge redistribution and d-band center shifts.[22,23] For example, Wu and colleagues constructed atomically dispersed Co–Fe dual sites embedded on N-doped porous carbon, which had an onset potential of 1.06 V and a half wave potential of 0.86 V in an acidic electrolyte.[24] The same group also reported a novel electrocatalyst with Co–Fe dual sites embedded in N-doped carbon nanotubes, which showed an onset potential of 1.15 V and a half wave potential of 0.954 V in alkaline solution.[25] Density functional theory (DFT) calculation results revealed that the Fe–Co dual sites could reduce the cleavage barrier energy of the O=O bond to achieve high activity and the preferential selectivity of the 4-electron transfer pathway in ORR.[24,25] In addition, Xiao *et al.* discovered that the anchoring of OH^- on the Co–Fe dual-atom centered $FeCoN_5$ site could enable an optimal e_g-orbital energy level for Fe and a favorable geometric configuration for the desirable O=O bridge adsorption, which significantly boosted the ORR performance.[26] Furthermore, other studies on binary M–N_x–C systems also show that the bimetallic architecture can elongate the O–O bond length to facilitate the bond cleavage, and the adjacent two metals can modulate the electronic interaction to eventually promote ORR activity.[27,28]

Herein, we report a facile strategy to synthesize atomically dispersed CoFe–N_x–C catalysts, using inexpensive phenol formaldehyde resin (PFR) spheres and NH_4Cl as co-anchors to maximize the reactive surface sites. Metal ions are adsorbed into the PFR spheres and initially anchored by surface N atoms and NH_4Cl. This complex is then pyrolyzed to form atomically dispersed CoFe–NC, in which NH_4Cl plays an additional role of forming pores in the carbon matrix. As a result, the CoFe–N_x sites are uniformly distributed on the surface of the nitrogen doped microporous carbon (NC) and the inner walls of the pores, which ensures the accessibility of the active sites. The atomically dispersed CoFe–N_x sites were characterized with atomic resolution high-angle annular dark-field scanning transmission electron microscopy (HAADF-STEM), X-ray absorption spectroscopy (XAS) and atomic pair distribution function (PDF) analysis. XAS studies show that the coordination motif of nitrogen with Co and Fe resembles N_3Co–FeN_3, with the Co atoms likely being responsible for the formation of this catalytic motif. The PDF analysis further indicates the longer range structural organization of Co and Fe atoms while modulating the overall structural coherence within the disordered carbon. DFT calculations reveal that the N_3Co–FeN_3 active motif acts as an excellent active center toward ORR on the slightly disordered carbon substrate. The as-prepared CoFe–NC catalyst exhibited a superior ORR performance compared to the Pt/C catalyst in alkaline media, thanks to the appropriate adsorption energies of the oxygenated species and the strong molecular orbital interactions from the atomic Co–Fe dimers, as revealed by the computational models. As an air cathode, CoFe–NC also demonstrated properties which outperformed Pt/C in our zinc–air battery experiments. While desirable properties were obtained using Co and Fe dual site catalysts, we envision that this synthetic route and subsequent characterization strategies are readily adaptable to a range of atomically dispersed M–N_x–C catalysts to enhance reactivities in a series of possible reactions.

Experimental

Materials

Cobalt chloride hexahydrate ($CoCl_2 \cdot 6H_2O$, AR) and ferric chloride hexahydrate (AR, $FeCl_3 \cdot 6H_2O$), 4-aminophenol (AR) and ammonium chloride (AR, NH_4Cl) were purchased from the Sinopharm Chemical Reagent Co., Ltd (Shanghai, China). Formaldehyde (AR, 37%), pluronic F-127 (AR), ammonium hydroxide (AR, 28%), ethanol (AR) and potassium hydroxide (95% KOH) were acquired from Energy Chemicals (Shanghai, China). Nitric acid (AR, 65% HNO_3) and perchloric acid (AR, 70% $HClO_4$) were procured from the Guangzhou Chemical Reagent Factory (Guangzhou, China). Commercial 20% Pt/C was obtained from Alfa Aesar. Nafion™ was acquired from Dupont (USA). All aqueous solutions were prepared using deionized (DI) water with a resistivity of 18.3 MΩ cm.

Synthesis of the phenol formaldehyde resin (PFR) nanospheres

1.5 g F-127 was first dissolved in 20 mL DI H_2O, then 0.5 g 4-aminophenol was added to the above solution, then the mixed solution was ultrasonically dispersed for 5 min. Secondly, 0.35 mL of formaldehyde and 0.3 mL NH_3 H_2O were diluted using 10 mL DI H_2O and added into the above mixed solution at room temperature, then heated to 80 °C and stirred for 18 h. Finally, the sample was washed with DI H_2O and dried at 35 °C for 12 h in the vacuum oven. NH_3 H_2O was used as a catalyst for phenolic resin condensation. The final sample was marked as PFR.

Preparation of atomically dispersed CoFe–NC, Co–NC, and Fe–NC

The typical preparation process of CoFe–NC was as follows; 0.5 mmol $CoCl_2 \cdot 6H_2O$ and 0.5 mmol $FeCl_3 \cdot 6H_2O$ were dissolved in 10 mL DI H_2O, then 100 mg PFR was added into the mixed solution and ultrasonically dispersed for 5 min. To promote the Co^{2+}, Fe^{3+} ions being uniformly and fully adsorbed by the PFR, the mixed solution needed to be slowly stirred at room temperature for 4 h. Subsequently, the above solution was freeze dried at −50 °C for 12 h, and the sample was marked as CoFe/PFR. CoFe/PFR and 4.0 g NH_4Cl were ground in an agate mortar for 10 min, and then carbonized at 900 °C

for 2 h with a heating rate of 2 °C min^{-1}. Finally, those CoFe particles that did not form a stable structure with NC were etched using 2 M HNO_3, and the sample was marked as CoFe–NC (the same sample of CoFe–NC-900 in Fig. S1,† and CoFe-35 in Fig. S2,† where 35 is the initial total metal loading percentage of Co and Fe). Samples with carbonization temperatures of 800 °C and 1000 °C were also prepared (CoFe–NC-800 and CoFe–NC-1000 in Fig. S1†). In addition, the method for preparing CoFe-25, CoFe-30, CoFe-40 and CoFe-45 (Fig. S2†) was similar to that of CoFe–NC (CoFe-35), with the amounts of $CoCl_2 \cdot 6H_2O$ being 0.3 mmol, 0.4 mmol, 0.6 mmol and 0.7 mmol, and the amounts of $FeCl_3 \cdot 6H_2O$ being 0.3 mmol, 0.4 mmol, 0.6 mmol and 0.7 mmol for CoFe-25, CoFe-30, CoFe-40 and CoFe-45, respectively. By setting the molar amount of total metal ions was = as 1.0 mmol and then adjusting the ratio of Co to Fe to 1 : 3 and 3 : 1, Co_3Fe–NC and $CoFe_3$–NC (Fig. S3†) was synthesized according to the preparation method of CoFe–NC (Co : Fe = 1 : 1). The method for preparing Co–NC and Fe–NC was the same as that of CoFe–NC; the difference is that for Co–NC the amount of $CoCl_2 \cdot 6H_2O$ was increased to 1 mmol and it was without $FeCl_3 \cdot 6H_2O$, and for Fe-NC the amount of $FeCl_3 \cdot 6H_2O$ was increased to 1 mmol and it was without $CoCl_2 \cdot 6H_2O$.

Preparation of OMC, NC and atomically dispersed CoFe–C

OMC was prepared by carbonizing the PFR at 900 °C with a heating rate of 2 °C min^{-1} for 2 h. NC was prepared by carbonizing the mixture of PFR (100 mg) and NH_4Cl (4.0 g) at 900 °C with a heating rate of 2 °C min^{-1} for 2 h. CoFe–C was synthesized according to the CoFe–NC method and the only difference was direct carbonization without NH_4Cl after freeze drying.

Details of the electrochemical measurements, characterization and simulation methods can be found in the ESI.†

Results and discussion

Synthesis, SEM and TEM characterization

CoFe–NC (Co–Fe dual sites on nitrogen doped microporous carbon) was first synthesized by following the route shown in Fig. 1a (see the ESI† for details). Briefly, the phenol formaldehyde resin (PFR) spheres were first prepared through the polycondensation of 4-aminophenol and formaldehyde with F-127, which served as the surfactant to control the size and as a structural direct agent for forming PFR.[29] Subsequently, Co^{2+} and Fe^{3+} ions were absorbed into the pores of the PFR by van der Waals forces, and initially anchored with nitrogen by coordination (termed as CoFe/PFR). CoFe/PFR and NH_4Cl were then mixed by grinding and carbonized under Ar atmosphere, followed by chemical etching in nitric acid to remove the inactive and unstable species. The catalyst (denoted as CoFe–NC) was then washed and dried for further catalytic testing and characterization.

The morphological changes during each step of the synthesis were monitored using scanning electron microscopy (SEM). As shown in Fig. 1b, PFR holds a well-defined pore structure with the diameter of the spheres being about 134 ± 27 nm. This carbon skeleton is mostly well preserved in the final product of CoFe–NC upon calcination at 900 °C, as depicted in Fig. 1c. However, there are some amorphous carbon layers formed on the surfaces of the carbon spheres. The N_2 adsorption–desorption isotherm of CoFe–NC can be found in Fig. 1d, where CoFe–NC possesses a large specific surface area of ~830 m^2 g^{-1}, a total pore volume of ~3.49 cm^3 g^{-1} and uniform micropores with pore diameters of ~1.86 nm. Transmission electron microscopy (TEM) was performed to investigate the bulk or nanoscale metals/metal oxides in CoFe–NC. As shown in Fig. 1e–g, nanoscale CoFe particles are not detected in CoFe–NC. Moreover, the X-ray diffraction (XRD) patterns (Fig. 1h) also do not show any diffraction peaks for Co, Fe or CoFe alloyed particles, nor their associated metal oxides, only two broad peaks at $2\theta = 24.3°$ and 43.2° associated with the microporous C.

It is important to note that F-127 is critical as the morphology control agent for forming the ordered pore structure of PFR. In the presence of F-127, formaldehyde and 4-aminophenol forms micelles that then solidified to yield a resols/F-127 composite by the cross-linking between 4-aminophenol and formaldehyde.[29] When F127 is partially removed with excess ethanol and deionized water, the ordered pore structure will be formed on the surface of PFR by the accumulation and rearrangement of small spherical micelles.[30] Previously it has been demonstrated that F-127 has a strong confinement effect which suppresses the agglomeration of Co atomic sites during thermal activation when forming $Co–N_4$.[31] Here, we are using F-127 to suppress metal agglomeration. Moreover, the introduction of NH_4Cl in the calcination process also plays a crucial role in the formation of the CoFe-NC. Typical SEM images of the OMC (PFR pyrolyzed at 900 °C without NH_4Cl), NC (PFR pyrolyzed at 900 °C with NH_4Cl) and CoFe–C (CoFe/PFR pyrolyzed at 900 °C without NH_4Cl) samples can be found in Fig. S4.† Without adding NH_4Cl, "naked" carbon spheres are obtained (OMC in Fig. S4a and CoFe–C in Fig. S4c†), but with the presence of NH_4Cl, amorphous carbon layers are formed on the surface of the carbon spheres (NC in Fig. S4b†). Fig. S4d† presents the N_2 adsorption–desorption isotherms of OMC-900, NC and CoFe–C. The specific surface areas, total pore volumes and pore diameters of OMC-900, NC, CoFe–C and CoFe-NC are summarized in Table S1.† Compared with OMC-900 and CoFe–C, NC and CoFe–NC possess higher specific surface areas and larger pore volumes. Such a phenomenon indicates that the introduction of NH_4Cl can etch the carbon matrix during pyrolysis to form micropores, which leads to the enhanced specific surface area. Therefore, NH_4Cl can not only provide an additional nitrogen source to anchor the Co and Fe atoms, but is also able to promote the formation of amorphous carbon layers on the surface of CoFe-NC and enhance the surface area and the pore volume as well. As a note, the abundant uniform micropores and large specific surface area in CoFe–NC are expected to maximize the density of the active sites and promote mass transport for electrocatalytic reactions.[32]

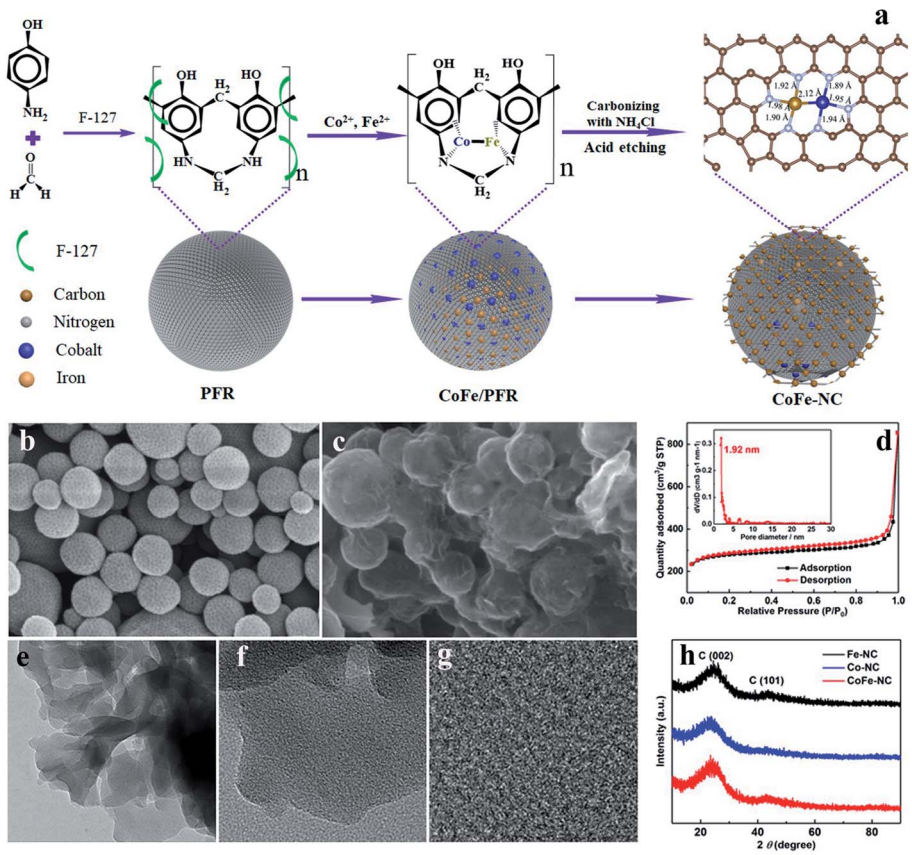

Fig. 1 (a) Schematic illustration of the synthesis of CoFe–NC; (b) and (c) typical SEM images of PFR and CoFe–NC, respectively; (d) the N_2 adsorption–desorption isotherms (inset is the pore size distribution) of CoFe–NC; (e–g) the typical TEM images of CoFe–NC with different magnifications; (h) the XRD patterns of Fe–NC, Co–NC and CoFe–NC.

HAADF-STEM, XANES, XEAFS analysis and PDF modeling

To further probe the atomic dispersity in CoFe–NC, high-angle annular dark-field scanning transmission electron microscopy (HAADF-STEM) was performed (Fig. 2a). A large number of Co and Fe atoms are present as bright spots and are well dispersed on the C support. The inset highlights that the majority of metal atoms in the HAADF-STEM are coupled together, indicating the formation of Co–Fe dual sites. This result was further verified by using electron energy-loss spectroscopy (EELS). As shown in Fig. S5,† when the electron beam was sputtered on the area of Fig. 2a in the white rectangle, both Fe and Co are present in the spectrum, indicating that the Fe and Co atoms coexist in the CoFe–NC catalyst. Note that a small amount of isolated Co or Fe sites are also observed in the HAADF-STEM image. The coordination between Co, Fe and N atoms can be examined by HAADF-STEM measurements in conjunction with EELS mapping. The corresponding EELS mapping (Fig. 2b) further shows that the Co and Fe atoms are dispersed as single atoms and diatoms in CoFe–NC, rather than as clusters or nanoparticles. In addition, Fig. S6a and b† reveal that Co and Fe single atoms are atomically dispersed in the Co–NC and Fe–NC samples, respectively, suggesting that this method can be applied to synthesize atomically dispersed monometallic catalysts as well. The surface composition and electronic structure of the CoFe–NC sample were then probed by XPS measurements. The XPS survey scan spectrum shows the coexistence of C (92.03 at%), N (6.74 at%), Co (0.73 at%) and Fe (0.50 at%) species in CoFe–NC (Fig. S7†). The corresponding weight percentages of the Co and Fe elements in CoFe–NC, estimated from XPS, are 3.39% and 2.15%, and to further confirm such values, inductively coupled plasmon-atomic emission spectroscopy (ICP-AES) was conducted and the results are summarized in Table S2.† It is worth noting that the actual Co and Fe content in Co–NC, Fe–NC and CoFe–NC determined from ICP-AES are lower than the values from XPS. This is mainly due to XPS being a surface sensitive detection technique, and in the above samples the metal atoms are enriched on the surface of the carbon substrate, resulting in the contents of the metal atoms detected by XPS being higher than those from ICP-AES.

The high resolution XPS N 1s spectra of CoFe-NC, OMC-900 and NC are illustrated in Fig. S8a.† For all of the samples, four sub-peaks corresponding to pyridinic N, pyrrolic N, graphitic N and oxidized N can be deconvoluted.[33] It is of particular note that the pyridinic N in OMC-900 and NC possessed identical binding energies (398.1 eV), while this peak in CoFe–NC shifts to 398.5 eV. The peak positions of the other N species in CoFe–NC are the same as those for OMC-900 and NC, indicating that the Co and Fe atoms are bonded by pyridinic N to form the

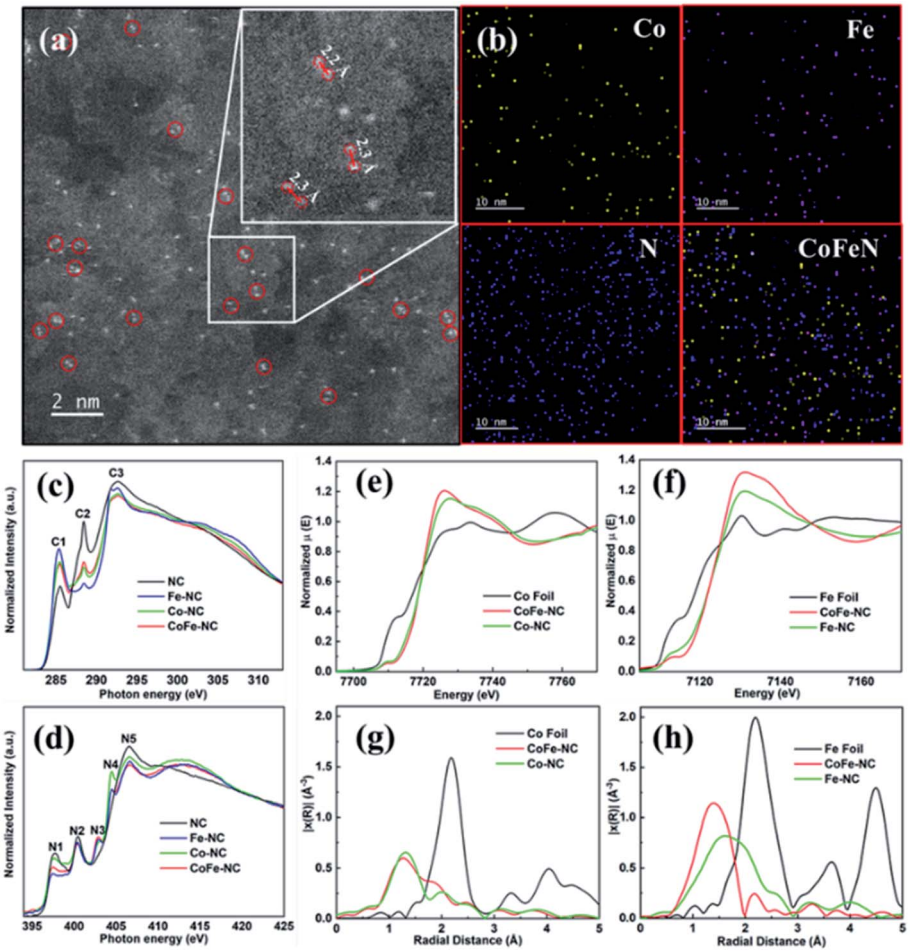

Fig. 2 (a) Atomic-resolution high-angle annular dark-field (AR-HAADF) scanning TEM image of CoFe–NC; (b) corresponding EELS mapping of Co, Fe, N and the composite image; (c) C K-edge and (d) N K-edge NEXAFS spectra of NC, Co–NC, Fe–NC and CoFe–NC; (e) Co K-edge and (f) Fe K-edge XANES spectra, (g) Co K-edge and (h) Fe K-edge EXAFS spectra of Co–NC, Fe–NC and CoFe–NC.

CoFe–N moieties. Fig. S8b† gives the concentrations of the four N species for the samples. This indicates that the concentration of pyridinic N in CoFe–NC (2.42 at%) is higher than those in OMC-900 (0.82 at%) and NC (1.63 at%), suggesting that CoFe–NC contains a large number of edge structure, which could generate plentiful edge nitrogen contained CoFe–N_x moieties. Moreover, the binding energies of the Co 2p (Fig. S9a†) and Fe 2p (Fig. S9b†) electrons in CoFe–NC are slightly shifted to higher values compared to those in Co–NC and Fe–NC, indicating that they have higher oxidation states.

To further probe the electronic structures of the catalysts, XAS measurements were performed at the K-edge of each element in our catalysts. The near edge X-ray absorption fine structure (NEXAFS) measurements at the C K-edge (Fig. 2c) exhibit peaks labeled C1 and C3 at 285.3 and 292.5 eV which are mainly derived from the aromatic C–C π* and C–C σ* transitions, respectively.[34] Compared to NC, Co–NC, Fe–NC and CoFe–NC exhibited obvious intensity increases of the C1 peaks and decreases of the C3 peaks, suggesting increases of the π-network electron densities in the catalyst atoms.[34] Noticeably, a sharp peak at 288.5 eV (C2) was detected for NC, Co–NC, Fe–NC and CoFe–NC, which is attributed to C–N bonding.[35] By contrast, the C2 peak intensity of NC was stronger than those of the Co–NC, Fe–NC and CoFe–NC catalysts, which is likely due to the partial removal of C–N–C moieties with the inclusion of the M–N_X–C sites.[36] The N K-edge NEXAFS spectra (Fig. 2d) exhibited five sharp peaks labeled N1, N2, N3, N4 and N5, which can be assigned to the pyridinic N π*, graphitic N, N–N, N–O and C=N σ* transitions, respectively.[37] Compared to NC, the intensities of the N1, N2 and N5 peaks decrease in Co–NC, Fe–NC, and CoFe–NC, while the N3 and N4 peaks show marked increases in intensity, implying the removal of C=N bonds and the formation of metal–N coordination after pyrolysis.[38]

The electronic structures and the local coordination environments of the metal atoms within CoFe–NC, Co–NC and Fe–NC were then examined at the K-edges of the respective metals. Fig. 2e shows the Co K-edge XANES spectra of CoFe-NC and Co-NC compared with a Co foil reference. It can be noted that CoFe-NC and Co-NC possessed higher intensity white lines compared to Co foil, indicating that non-metallic Co exists in the atomically dispersed samples.[39] In addition, the white line intensity of CoFe–NC is slightly higher than that of Co–NC, likely due to Co–

Fe intermetallic electron transfer between the Co and Fe atoms in the coupled metal system and/or through interactions with neighboring N atoms. Similarly, the Fe K-edge XANES of CoFe–NC and Fe–NC indicate that non-metallic iron or bulk oxidized Fe is obtained, exhibiting similar features of previously reported atomically dispersed Fe (Fig. 2f).[40] The white line intensity of the Co–Fe system again is higher overall while coupled with a decrease in the pre-edge feature, indicating that the Co–Fe dual site catalyst is losing electron density when paired together. Bader charge analysis of the different catalyst configurations (Table S3†) indicates an increased removal of charge from both the Fe and Co atoms in the dual site CoFe, as compared to the single metal sites. This decrease in the charge of the metal atoms is coupled with an increase in electron accumulation on the N atoms, which is consistent with our XANES findings. Additional discussion on the DFT calculations of these materials can be found below.

The Fourier-transformed (FT) k^2-extended X-ray absorption fine structure (EXAFS) spectra for the Fe and Co K-edges are shown in Fig. 2g and h, along with those of the reference metal foils (not corrected for phase shift). Corresponding k^2-space data is provided in Fig. S10.† At the Co K-edge, the dominant peaks are positioned at 1.32 Å and 1.26 Å for Co–NC and CoFe–NC, respectively, and arise from the local Co–N coordination environment. Lower magnitude features at higher radial distances can be observed for both Co–NC and CoFe–NC, which likely reflect the nearest neighbor distances (NNDs) to the carbon-based coordination spheres around the Co atoms and binary metallic pairs in CoFe–NC. The Fe K-edge EXAFS spectra provide similar information, with Fe–N coordination distances positioned at 1.56 Å and 1.38 Å for Fe–NC and CoFe–NC, respectively. The main EXAFS feature in Fe–NC is notably broader with a likely additional EXAFS contribution at 1.87 Å. Note that, as shown in the EXAFS data for both metals, the binary metal system produces a shorter M–N NND, indicating that the secondary metal is directly influencing the immediate coordination environment.

The EXAFS data was then modeled using backscattering contributions from known metal coordination complexes, as described in the experimental section. The modelling results are summarized in Table S4 and shown in Fig. S11.† For Co–NC, a Co–N coordination number (CN) of 2.74 ± 0.46 was calculated, indicating a near Co–N_3 local coordination environment. An average Co–N NND of 1.93 ± 0.01 Å was obtained through modeling, which is consistent with similar previously reported catalytic sites.[39] To obtain a satisfactory EXAFS fit, 2nd and 3rd coordination spheres with C were modeled with the respective CNs of 4.66 ± 1.73 and 5.04 ± 2.16 at distances of 2.63 ± 0.04 Å and 2.84 ± 0.04 Å. Fe–NC was modelled in a similar fashion and exhibits higher CNs for Fe–N and the first Fe–C coordination sphere. The results are summarized in Table S5 and shown in Fig. S11.† This outcome indicates that the presence of metal species influences the formation and structure of the catalyst, which could have implications for the overall catalytic activity and catalyst design.

The binary CoFe-NC was also modeled using information from both the Fe and Co K-edges simultaneously (Table S4 and S5†). As shown in Fig. S11,† the CN corresponding to the metal–metal is found to be 1.02 ± 0.21 at a NND of 2.07 ± 0.02 Å. This result indicates that the majority of metal atoms form dimers during synthesis, albeit with a moderate uncertainty that arises from the low amounts of non-dimerized metals. The corresponding Fe–N and Co–N CNs are similar, with a Fe–N CN of 3.24 ± 0.48 and a Co–N CN of 3.23 ± 0.46 at respective NNDs of 1.94 ± 0.01 Å and 1.85 ± 0.01 Å. The positions of the M–N bonds are similar in the binary catalyst as compared to their monometallic counterparts with a MN_3-type geometry. The C lattice in NC is significantly disordered here as well, as low Co–C CNs are again obtained, while this distance could not be modeled from the Fe K-edge. Overall, these results showcase that the largely coupled binary catalyst obtained through the templating methodology used here provides a means to create unique and tunable catalytic active sites.

While EXAFS can provide localized structural information around the desired element, the longer-range structure is difficult to ascertain. This missing structural information may be critically important, as the dispersion of metal atoms and its associated effect on the matrix structure likely plays a major role in determining the material's catalytic properties. Given the known influence of structural defects on the electronic structure of nanoscale carbon materials,[41–43] understanding the structure of both the local catalyst environment and the host may prove useful in understanding the catalytic properties of M–N_x–C materials. To this end, we probed the atomically dispersed catalysts using high-energy X-ray diffraction (HE-XRD) coupled to atomic pair distribution function (PDF) analysis. HE-XRD/PDF analysis is an ideal structural characterization method for nanoscale materials,[44] as atomic pair distances of >30 Å can be determined through diffraction experiments without the need for long range order.[45] If an appropriate background is available, a differential PDF (dPDF) can be obtained to probe the structure of minority species within a large lattice.[46] Here, we use dPDF to better understand the influence of the catalyst structure by subtracting out all non-metal atomic pairs using the NC PDF.

As shown in Fig. 3a, the longer range ordering, resulting from the metal-derived atomic pairs, differs across all three atomically dispersed materials. Both Co–N_x and CoFe–N_x exhibit a feature at 1.92 Å, which arises from M–N and agrees with our EXAFS results. The first dPDF peak in Fe–N_x occurs at 2.14 Å, which is also present in CoFe–N_x. This feature again agrees well with the Fe–N NNDs from the EXAFS modeling of the Fe K-edge for Fe–N_x and Co–Fe in CoFe–N_x. At longer atomic-pair distances, structural changes can be clearly observed from the dPDF. Most notably are the dPDF peaks found within Fe–N_x from ~2.5–3.5 Å, which are pronouncedly different from those observed in Co–N_x and CoFe–N_x. This finding suggests that interactions within the carbon lattice between Co and Fe are quite different, and that Co has a stronger influence in forming the eventual final structure of the catalysts. In addition, Co–N_x and CoFe–N_x exhibit peaks that align more closely with NC, which is essentially a graphite-like lattice, while Fe–N_x tends to shift away from this lattice. Observations from the longer range dPDFs (Fig. 3b) show the

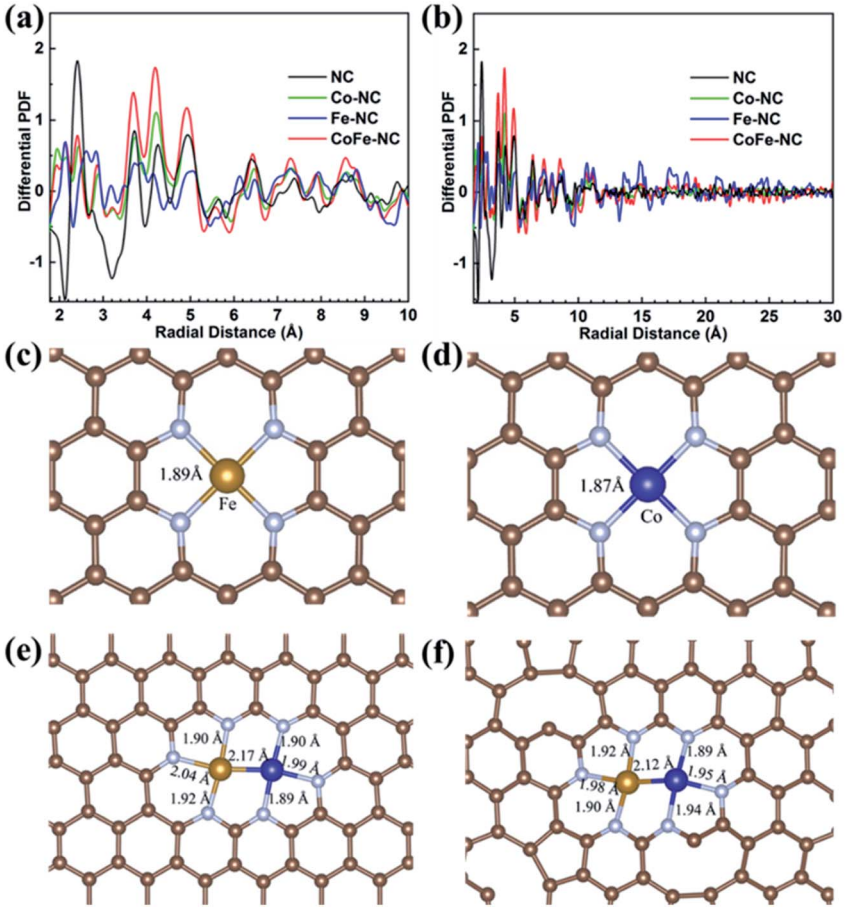

Fig. 3 Differential atomic pair distribution function (dPDF) analysis at 10 Å (a) and 30 Å (b) of the Co–NC, Fe–NC and CoFe–NC samples. The top view of the optimized structures for (c) single atom Fe on the NC substrate in the Fe–NC sample and (d) single atom Co on the NC substrate in the Co–NC sample. (e) and (f) show the Co–Fe dimer atoms on (e) the highly ordered NC substrate and (f) the slightly disordered NC substrate. The C and N atoms are in brown and cyan, respectively, and only the Fe and Co atoms in (c) and (d) are labelled for clarity. The distances of Fe–N and Co–N are labelled near the bond.

relatively increased overall atomic order in Fe–N_x, further showcasing the differences of the NC host structure with the inclusion of Fe and/or Co. Overall, the dPDF analysis provides the necessary expanded insights into the structure of the atomically dispersed catalysts beyond the local coordination of the metal atoms to help better understand the structure/function relationships for these materials.

To further confirm the structural findings, DFT calculations were then conducted. The optimized structures of the single-atomic metals on the NC substrates are shown in Fig. 3c–f. It can be observed in Fig. 3c and d that the center single Fe (Co) atom is coordinated to the 4 nearest N atoms, and the average Fe–N (Co–N) distance is measured to be 1.89 Å (1.87 Å). These values are consistent with the fitting of the EXAFS data (2.00 Å for Fe–N and 1.93 Å for Co–N), suggesting the suitability of the models built here. We further evaluated the structure of the Co–Fe dimer on the NC substrate. For the highly ordered structure, the average Fe–N, Co–N and Co–Fe distances were computed to be 1.95 Å, 1.92 Å and 2.17 Å, respectively, as seen in Fig. 3e. For the slightly distorted structure shown in Fig. 3f, the above values are predicted to be 1.93 Å, 1.93 Å and 2.12 Å, respectively. These values are consistent with those from the experimental EXAFS and PDF measurements (1.94 Å for Fe–N, 1.85 Å for Co–N and 2.07 Å for Co–Fe). To further test the validity of the DFT simulations, XANES calculations we performed using the DFT structures as the input (see the ESI† for more details). The calculated XANES spectra (Fig. S12†) are in good agreement with the experimental XANES reported in Fig. 2 and are consistent with previously reported materials.[16,47]

Electrocatalytic ORR activity and zinc–air battery test

The ORR performances of the catalysts were evaluated using a rotating ring-disk electrode (RRDE) in O_2-saturated 0.1 M KOH solution. It is well known that the carbonization temperature also has a great influence on the catalytic performance. The catalysts were pyrolyzed at 800 °C (CoFe–NC-800), 900 °C (CoFe–NC-900) and 1000 °C (CoFe–NC-1000) and the ORR performances are illustrated in Fig. S1.† It can be noted that CoFe–NC-900 possesses the most outstanding half wave potential of 0.94 V, compared with 0.87 V for CoFe–NC-800 and 0.88 V for CoFe–NC-1000. Based on the above results, the calcination temperature of 900 °C was chosen as the optimal temperature

for preparing the CoFe–NC catalyst. To achieve the optimal performance of the atomically dispersed catalyst with Co–Fe dual sites, we investigated the effects of the weight percentages of Co and Fe on the catalytic activity. By setting the Co-to-Fe molar ratio as 1 : 1, the half wave potential of the catalysts first increased then decreased with the increasing of the metal amount (Fig. S2†). When the weight percentage of Co and Fe increased to 25%, 30% and 35%, the half-wave potential gradually increased to 0.78 V, 0.82 V and 0.94 V, respectively, indicating that the effective active sites were gradually enriched, but when continuously increasing the weight percentage to 40% and 45%, the half wave potential dropped to 0.86 V and 0.82 V, respectively, indicating that an excessive metal amount might led to aggregation of the single atom sites. Subsequently, we further explored the relationship between the Co-to-Fe molar ratio and the electrocatalytic activity. As shown in Fig. S3,† the catalytic performance of the samples first increased then declined with the decrease of the Co content, and the best performance can be obtained when the molar ratio of Co-to-Fe is 1 : 1 (CoFe–NC, $E_{1/2} = 0.94$ V). This suggests that the catalyst probably has the most appropriate adsorption energy for oxygen molecules when the ratio of Co-to-Fe is 1 : 1.

The polarization curves of Co–NC, Fe–NC, CoFe–NC, and Pt/C are shown in Fig. 4a. The half wave potential of CoFe–NC (0.94 V) is higher than those of Co–NC (0.80 V) and Fe–NC (0.83 V) and, more intriguingly, is 90 mV higher than that of Pt/C (0.85 V). The ORR performance of CoFe–NC was further evaluated and compared with Pt/C. Fig. S13† shows the RDE voltammograms recorded with different rotation rates for CoFe–NC and Pt/C. Note that the current densities increased with the increase of the rotation rate for both samples, where in the mixed kinetics/diffusion controlled region, excellent linearities with rather consistent slopes were acquired in the Koutecky–Levich (K–L) plots for both samples. These results indicate a first order reaction kinetics for ORR with respect to the oxygen concentration in the solution. Fig. 4b shows the Tafel plots for CoFe–NC and Pt/C, where CoFe–NC exhibits a smaller Tafel slope value of 68 mV dec^{-1} than that of Pt/C (76 mV dec^{-1}) in alkaline solution, implying that CoFe–NC possesses faster reaction kinetics. In addition, the electron transfer number and yield of H_2O_2 for both CoFe–NC and Pt/C in the potential range of 0.2–0.8 V were calculated by eqn (1) and (2).† As illustrated in Fig. 4c, CoFe–NC has an electron transfer number of 3.90–3.92, comparable to Pt/C (3.88–3.92). In addition, the H_2O_2 yield of CoFe–NC (3.81–3.92%) is slightly lower than that of Pt/C (4.22–9.23%), suggesting improved ORR selectivity in alkaline solution. Finally, the durability of CoFe–NC was evaluated and compared with Pt/C by amperometric *i–t* curves at 0.85 V with a rotation speed of 900 rpm. As shown in Fig. 4d, after 16 hours of continuous operation, CoFe–NC maintains 92% of the initial current, which is much higher than that of Pt/C (86%), indicating the improved long-term stability of CoFe-NC over this period of time.

Moreover, the ORR performance of CoFe–NC was also assessed and compared with Pt/C in 0.1 M $HClO_4$. Fig. S14a† shows the polarization curves, where CoFe–NC possesses a half wave potential of 0.80 V, which is higher than those of Co–NC and Fe–NC, but slightly inferior to that of the Pt/C catalyst (0.85 V). The 50 mV difference is reasonable, as Pt/C possessed incomparable performance in acid media. Fig. S15† depicts the current density change with the change of rotation rate, with highly linear responses observed in the K–L plots for both samples, suggesting first-order reaction kinetics for both samples. The subsequently extrapolated Tafel plots are presented in Fig. S14b,† where CoFe–NC exhibited a slightly lower but comparable Tafel slope value to Pt/C, an indication of the comparable intrinsic catalytic behaviors. In addition, CoFe–NC also demonstrated close values of the numbers of electron transferred and yields of H_2O_2 with those of Pt/C (Fig. S14c†). Lastly, in the *i–t* test (Fig. S14d†), CoFe–NC retained 88% of its initial current, which is superior to that of Pt/C (76%). This shows that CoFe–NC has improved long-term durability over Pt/C in acidic media as well.

It is worth noting that the ORR performance of CoFe–NC in alkaline media is markedly improved over recently reported M–N_x–C based atomically dispersed catalysts (see Table S6†). We attribute the improved ORR performance in alkaline media to the well-defined atomically dispersed structure of CoFe–NC, with Co–Fe dual sites enriched onto the surface of the carbon spheres. The uniform micropores in the carbon substrate are beneficial for the adsorption of Fe^{3+} and Co^{2+} ions, which can increase the loading of the active sites (4.78 wt% from ICP-AES). In addition, the large specific surface area of CoFe–NC (Fig. 1d, 830 m^2 g^{-1}) can not only enhance the accessibility of the O_2 molecules, but also imparts Co–Fe dual sites which are homogeneously dispersed (shown by the HAADF-STEM image in Fig. 2a), which improve the utilization of the active sites. The addition of NH_4Cl in the synthesis as an additional nitrogen source dramatically increased the content of pyridinic N (shown in Fig. S5b†) in CoFe–NC, where pyridinic N can enhance the surface wettability and boost the onset potential and half-wave potential.[48] Finally and most importantly, the unique coordination structure of the sample (N_3Co–FeN_3, shown in Fig. S8†) can lead to the charge redistribution of the neighboring atoms, resulting in a synergistic effect between the dual active sites (CoN_3 and FeN_3), which eventually promotes oxygen activation by weakening the O=O bond.[24,25]

To gain some insight into the mechanism, we first calculated the adsorption of a single O_2 molecule on substrates decorated with transition metals. The relaxed structures are shown in Fig. S16.† The O_2 molecule preferentially adsorbs above the transition metals through a side-on mode. Upon chemisorption, the O=O bond elongates from 1.21 Å in the isolated gas state to 1.39 Å for the Fe SA, 1.35 Å for the Co SA and 1.44 Å for the Co–Fe dimer. The adsorption free energies were calculated to be −0.50 eV for the Fe SA and 0.29 eV for the Co SA. Significantly, the adsorption free energies for the O_2 molecule on the Co–Fe sites were computed to be −1.02 eV and −1.70 eV for the ordered and disordered substrates, respectively. The more negative adsorption energies and the longer O=O bond suggest an increased interaction between the O_2 molecule and the Co–Fe dimer sites, implying an improved ORR performance, which is consistent with the findings of Shi *et al.*[49]

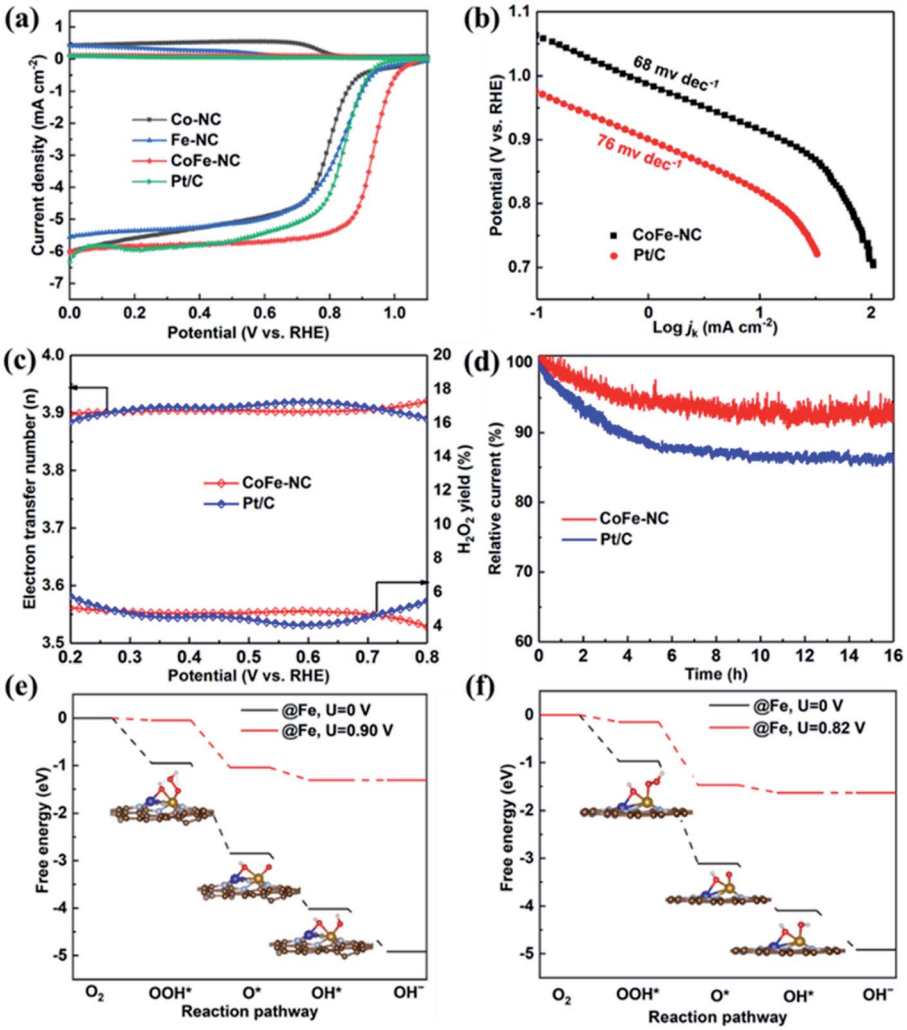

Fig. 4 The ORR performances of the different catalysts. (a) The LSV curves of Co–NC, Fe–NC, CoFe–NC and Pt/C measured in O_2-saturated 0.1 M KOH with a rotation rate of 1600 rpm; (b) Tafel plots of CoFe–NC and Pt/C; (c) the H_2O_2 yield and electron transfer numbers of CoFe–NC and Pt/C; (d) the *i*–*t* curves of CoFe–NC and Pt/C at 0.85 V and 900 rpm. Free energy diagram of ORR at each elementary step on the (e) Fe site of Co–Fe dual atoms with adsorbed OH on the slightly disordered NC substrate and (f) Fe site of Co–Fe dual atoms with adsorbed OH on the ordered NC substrate. The optimized structures are also shown as insets in the figures.

The plots of the charge density difference between the adsorbed O_2 molecule and the substrates are shown in Fig. S17,† where the accumulation of electrons between the metal and O suggests the formation of M–O σ bonds. From the Bader charge analysis (see Table S3† for the values), one can observe a stronger electron loss for the Co–Fe dimer sites compared to SA Fe and SA Co. In agreement with the correlation between a less positive metal center and enhanced ORR activity, suggested by Li *et al.*,[50] the Co–Fe dimer sites on the slightly disordered NC are expected to display a better ORR performance compared to the other systems studied.

The ORR mechanism for the Co–Fe dimer was then investigated following Nørskov's work.[51] As shown in Fig. S18a,† each reaction step for the Co–Fe sites on the highly ordered NC is exothermic. However, the free energy of the OH* formation reaction from O* is low, suggesting that it is rate-limiting. The reaction free energy for the Co–Fe dimer sites on the slightly disordered NC is shown in Fig. S18b,† where the OH* removal step is endothermic. As suggested by Li *et al.*,[25] OH* is anchored at the Co–Fe bridge during ORR. We will denote the OH* adsorbed on the Co–Fe dimer sites as CoFe–OH, as seen in the inset of Fig. S18b†. The ORR free energy diagram at the Fe site of CoFe–OH on disordered NC is shown in Fig. 4e. Each ORR step is exothermic and the limiting potential (the maximum external potential at which the ORR processes are still exothermic) is predicted to be 0.90 V, a value even higher than that of Pt (0.79 V).[25] The free energy diagram at the Co site is displayed in Fig. S19a,† showing a limiting potential of only 0.58 V. After comparing the total energy of each intermediate adsorbed on the substrate, we can conclude that the ORR steps are likely to take place at the Fe site because of the lower computed energies. As a comparison, we also explored the ORR mechanism at the Fe site of CoFe–OH on highly ordered NC and show the results in Fig. 4f. It can be noticed that the limiting potential is 0.82 V,

lower than that of the disordered one. We must also observe that the limiting potentials for the Co–Fe dimer sites on highly ordered and slightly disordered NC are higher than those of SA Fe (0.54 V) and SA Co (0.81 V) (shown in Fig. S19b and c†), suggesting synergy between the Fe and Co in the Co–Fe dimer. Furthermore, the disorder of the NC substrate appears to make additional contributions to the ORR as an identical dimer on a slightly disordered substrate shows better activity compared to that on the highly ordered substrate.

The interaction between an adsorbed O_2 molecule and the transition metal atoms can be better understood using the molecular orbital theory, as shown in Fig. S20.† The calculations show that a strong π bond (the in-phase combination of the d_{xz} orbital of Fe or Co and one π^* orbital of O_2) and a weak δ bond (the in-phase combination of the d_{xy} orbital of Fe or Co and the other π^* orbital of O_2)[52] form in the structure with only one single metal atom catalyst, as seen in Fig. S20a.† However, in the presence of the Co–Fe dimer, two strong π bonds are formed. These two π bonds consist of the in-phase and out-of-phase combinations of the d_{z^2} orbitals of Fe and Co interacting with the π^* orbital of O_2, as seen in Fig. S20b.† The distortion of the O=O bond matches the in-phase combination with the d_{z^2} orbital to form the π bond. Detailed visualizations of the orbital interactions using the principal interacting spin orbitals (PISO)[53] are shown in Fig. S21–S26.† As suggested by Lin *et al.*,[53] the sum of all PISO-based bond indices can be regarded as the bond order, which can be further used to compare the bonding strengths of the adsorbate O_2 with different substrates. As a result, the indices were calculated to be 2.15, 1.91 and 2.41 for the SA Fe, SA Co, and the Co–Fe dimer, respectively, suggesting the strong interactions of the CoFe dimer with the substrates. These values are also consistent with the above analysis, supporting the conclusion that the Co–Fe dimer has the best ORR performance among the materials studied.

The excellent ORR performance of the CoFe–NC catalyst inspired us to explore its practical application in zinc–air batteries (ZABs). A primary ZAB was constructed by using zinc foil as the anode, CoFe–NC as the air cathode and 0.2 M $Zn(OAc)_2$ in 6 M KOH as the electrolyte. The commercial Pt/C catalyst was employed to compare the discharge capability of the ZAB with CoFe–NC, while for the integrated charge and discharge test, a ZAB performance comparison was made between the CoFe–NC + IrO_2 catalyst and the Pt/C + IrO_2 catalyst. Fig. 5a presents the discharge polarization curves and power densities, where the CoFe–NC modified ZAB exhibits a power density of 115 mW cm^{-2}, which is much larger than that of the Pt/C decorated ZAB (85 mW cm^{-2}). Meanwhile, as demonstrated in Fig. 5b, the specific capacity of the CoFe–NC modified ZAB is 791 mA h g^{-1}, which is also higher than that of the Pt/C decorated ZAB (707 mA h g^{-1}). Subsequently, the long-term stability of the CoFe–NC + IrO_2 and Pt/C + IrO_2 air cathodes were evaluated at 10 mA cm^{-2} with each cycle of 10 min (Fig. 5c). For the CoFe–NC + IrO_2 based battery, the discharge voltage remains almost constant at 1.2 V for about 80 h, and the charge voltage is kept at 2.0 V for about 70 h but gradually increases to 2.2 V at 80 h. In comparison, both the discharge and charge voltages can only remain stable for 30 h and increase

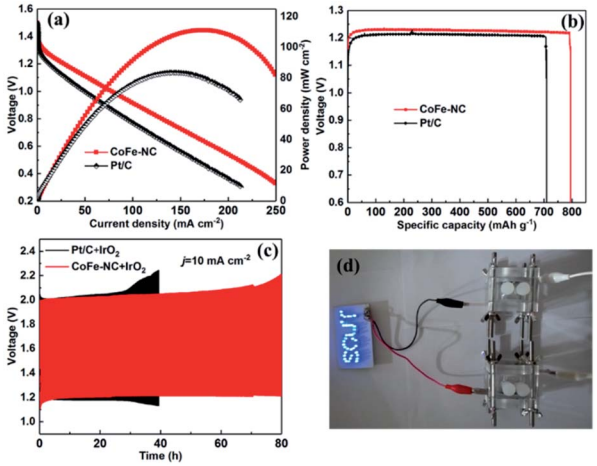

Fig. 5 (a) The discharge polarization curves and their corresponding power density curves with CoFe–NC and Pt/C as the air cathodes; (b) the discharge specific capacities of the CoFe–NC and Pt/C air cathodes at 10 mA cm^{-2}; (c) the charge–discharge plots of the ZABs based on the CoFe–NC + IrO_2 air cathode and Pt/C + IrO_2 air cathode; (d) the photograph of blue LEDs ($V \approx 3.0$ V) powered by two liquid Zn–air batteries with CoFe–NC air cathodes connected in series.

drastically at 40 h for the Pt/C + IrO_2 based battery. Lastly, two ZAB cells with the CoFe–NC air cathode connected in series can light up blue LED lamps (with a voltage of ~3.0 V, shown in Fig. 5d), showing that this battery is a promising power device for practical application. Moreover, the performance of the CoFe–NC based battery has exceeded or at least is comparable to those of recently documented M–N–C atomically dispersed catalysts, and the detailed comparisons regarding the power density, specific capacity and charge–discharge stability are summarized in Table S7.† The above results fully validate that CoFe–NC could be a promising alternative for the Pt/C catalyst in practical ZAB implementation as well.

Conclusion

In summary, we developed a facile strategy to prepare an atomically dispersed catalyst with Co and Fe dual sites enriched onto the surface of microporous carbon. Such a strategy can impart the maximal exposure of Co and Fe dual sites and leads to a high utilization of the active sites. As a result, the as-prepared CoFe–NC catalyst exhibited a superior ORR performance compared to the Pt/C catalyst in alkaline media. As an air cathode, CoFe–NC also outperformed Pt/C in the primary zinc–air battery test. More importantly, XAS measurements show that the bimetallic atoms regulate each other's electronic structure and directly affect the coordination environment, while the PDF analysis demonstrates that the metal atoms can tune the lattice structure of the NC, likely modifying its electronic properties. DFT calculations reveal that the atomic Co–Fe dimers lie on the slightly disordered NC rather than a highly ordered substrate, which agrees with our synchrotron structural analysis, and indicates that such configurations can provide the appropriate adsorption free energies of the oxygenated species, hence

promoting the ORR process and the primary zinc–air battery performance. This study not only provides a new facile strategy for preparing atomically dispersed dual metal site catalysts, but also clearly elucidates the metal–substrate interaction and unravels its impact on the catalytic performance. We envision that the findings here will be beneficial for the future rational design of atomically dispersed catalysts toward ORR and beyond.

Author contributions

Kai Wang: conceptualization, methodology, investigation, formal analysis, writing – original draft. Jiapeng Liu: methodology, theoretical calculations, writing – original draft. Zhenghua Tang: conceptualization, resources, writing – review & editing, funding support. Ligui Li: investigation. Zheng Wang: investigation. Muhammad Zubair: investigation. Francesco Ciucci: resources, theoretical calculation, writing – review & editing, funding support. Lars Thomsen: investigation, resources. Joshua Wright: investigation, resources. Nicholas M. Bedford: investigation, resources, writing – review & editing, funding support.

Conflicts of interest

The authors declare that they have no known competing financial interests or personal relationships that could have appeared to influence the work reported in this paper.

Acknowledgements

This study was supported by the Research Fund Program of the Key Laboratory of Fuel Cell Technology of Guangdong Province. Z. T. is grateful for the financial support from the Guangzhou Science and Technology Plan Projects (No. 201804010323) and the Guangdong Natural Science Funds for Distinguished Young Scholars (No. 2015A030306006). F. C. gratefully acknowledges the support of the Hong Kong Innovation and Technology Fund (No. ITS/292/18FP), the Research Grants Council of Hong Kong (16207615, 16227016, and 16204517) and the Guangzhou Science and Technology Program (No. 201807010074). This research used the 10-BM and 11-ID-B beamlines of the Advanced Photon Source, a U.S. Department of Energy (DOE) Office of Science User Facility operated for the DOE Office of Science by the Argonne National Laboratory under Contract No. DE-AC02-06CH11357. 10-BM is further supported by the DOE and the Materials Research Collaborative Access Team member institutions. M. Z. acknowledges the scholarship support from the Scientia PhD Scholarships program at UNSW. We would like to thank Leighanne Gallington for assistance with the experiments at 11-ID-B. NEXAFS measurements were performed on the SXR beamline at the Australian Synchrotron, part of the Australian Nuclear Science and Technology Organisation (ANSTO) and funded by the Australian Government. N.M.B acknowledges the partial financial support from the Faculty of Engineering at UNSW and travel funding provided by the International Synchrotron Access Program managed by the Australian Synchrotron.

References

1 M. Lefevre, E. Proietti, F. Jaouen and J. Dodelet, *Science*, 2009, **324**, 71–74.
2 J. Suntivich, H. A. Gasteiger, N. Yabuuchi, H. Nakanishi, J. B. Goodenough and Y. Shaohorn, *Nat. Chem.*, 2011, **3**, 546–550.
3 C. Tang and Q. Zhang, *Adv. Mater.*, 2017, **29**, 1604103.
4 C. Wang, N. M. Markovic and V. R. Stamenkovic, *ACS Catal.*, 2012, **2**, 891–898.
5 L. Dai, Y. Xue, L. Qu, H.-J. Choi and J.-B. Baek, *Chem. Rev.*, 2015, **115**, 4823–4892.
6 X. X. Wang, M. T. Swihart and G. Wu, *Nat. Catal.*, 2019, **2**, 578–589.
7 Y. Chen, S. Ji, C. Chen, Q. Peng, D. Wang and Y. Li, *Joule*, 2018, **2**, 1242–1264.
8 Y. He, S. Hwang, D. A. Cullen, M. A. Uddin, L. Langhorst, B. Li, S. Karakalos, A. J. Kropf, E. C. Wegener, J. Sokolowski, M. Chen, D. Myers, D. Su, K. L. More, G. Wang, S. Litser and G. Wu, *Energy Environ. Sci.*, 2019, **12**, 250–260.
9 G. Wu, K. L. More, C. M. Johnston and P. Zelenay, *Science*, 2011, **332**, 443–447.
10 Y. Chen, S. Ji, Y. Wang, J. Dong, W. Chen, Z. Li, R. Shen, L. Zheng, Z. Zhuang, D. Wang and Y. Li, *Angew. Chem., Int. Ed.*, 2017, **56**, 6937–6941.
11 H.-W. Liang, W. Wei, Z.-S. Wu, X. Feng and K. Müllen, *J. Am. Chem. Soc.*, 2013, **135**, 16002–16005.
12 N. R. Sahraie, U. I. Kramm, J. Steinberg, Y. Zhang, A. Thomas, T. Reier, J.-P. Paraknowitsch and P. Strasser, *Nat. Commun.*, 2015, **6**, 8618.
13 X. Wan, X. Liu, Y. Li, R. Yu, L. Zheng, W. Yan, H. Wang, M. Xu and J. Shui, *Nat. Catal.*, 2019, **2**, 259–268.
14 A. Zitolo, N. Ranjbar-Sahraie, T. Mineva, J. Li, Q. Jia, S. Stamatin, G. F. Harrington, S. M. Lyth, P. Krtil, S. Mukerjee, E. Fonda and F. Jaouen, *Nat. Commun.*, 2017, **8**, 957.
15 J. Li, M. Chen, D. A. Cullen, S. Hwang, M. Wang, B. Li, K. Liu, S. Karakalos, M. Lucero, H. Zhang, C. Lei, H. Xu, G. E. Sterbinsky, Z. Feng, D. Su, K. L. More, G. Wang, Z. Wang and G. Wu, *Nat. Catal.*, 2018, **1**, 935–945.
16 H. Fei, J. Dong, Y. Feng, C. S. Allen, C. Wan, B. Volosskiy, M. Li, Z. Zhao, Y. Wang, H. Sun, P. An, W. Chen, Z. Guo, C. Lee, D. Chen, I. Shakir, M. Liu, T. Hu, Y. Li, A. I. Kirkland, X. Duan and Y. Huang, *Nat. Catal.*, 2018, **1**, 63–72.
17 J. Li, S. Chen, N. Yang, M. Deng, S. Ibraheem, J. Deng, J. Li, L. Li and Z. Wei, *Angew. Chem., Int. Ed.*, 2019, **58**, 7035–7039.
18 F. Li, G.-F. Han, H.-J. Noh, S.-J. Kim, Y. Lu, H. Y. Jeong, Z. Fu and J.-B. Baek, *Energy Environ. Sci.*, 2018, **11**, 2263–2269.
19 M. Xiao, J. Zhu, G. Li, N. Li, S. Li, Z. P. Cano, L. Ma, P. Cui, P. Xu, G. Jiang, H. Jin, S. Wang, T. Wu, J. Lu, A. Yu, D. Su and Z. Chen, *Angew. Chem., Int. Ed.*, 2019, **58**, 9640–9645.

20 E. Luo, H. Zhang, X. Wang, L. Gao, L. Gong, T. Zhao, Z. Jin, J. Ge, Z. Jiang, C. Liu and W. Xing, *Angew. Chem., Int. Ed.*, 2019, **58**, 12469–12475.
21 M. Xiao, L. Gao, Y. Wang, X. Wang, J. Zhu, Z. Jin, C. Liu, H. Chen, G. Li, J. Ge, Q. He, Z. Wu, Z. Chen and W. Xing, *J. Am. Chem. Soc.*, 2019, **141**, 19800–19806.
22 H. Sun, M. Wang, S. Zhang, S. Liu, X. Shen, T. Qian, X. Niu, J. Xiong and C. Yan, *Adv. Funct. Mater.*, 2021, **31**, 2006533.
23 J. Wang, L. Gan, W. Zhang, Y. Peng, H. Yu, Q. Yan, X. Xia and X. Wang, *Sci. Adv.*, 2018, **4**, eaap7970.
24 J. Wang, Z. Huang, W. Liu, C. Chang, H. Tang, Z. Li, W. Chen, C. Jia, T. Yao, S. Wei, Y. Wu and Y. Li, *J. Am. Chem. Soc.*, 2017, **139**, 17281–17284.
25 J. Wang, W. Liu, G. Luo, Z. Li, C. Zhao, H. Zhang, M. Zhu, Q. Xu, X. Wang, C. Zhao, Y. Qu, Z. Yang, T. Yao, Y. Li, Y. Lin, Y. Wu and Y. Li, *Energy Environ. Sci.*, 2018, **11**, 3375–3379.
26 M. Xiao, Y. Chen, J. Zhu, H. Zhang, X. Zhao, L. Gao, X. Wang, J. Zhao, J. Ge, Z. Jiang, S. Chen, C. Liu and W. Xing, *J. Am. Chem. Soc.*, 2019, **141**, 17763–17770.
27 Z. Lu, B. Wang, Y. Hu, W. Liu, Y. Zhao, R. Yang, Z. Li, J. Luo, B. Chi, Z. Jiang, M. Li, S. Mu, S. Liao, J. Zhang and X. Sun, *Angew. Chem., Int. Ed.*, 2019, **58**, 2622–2626.
28 G. Yang, J. Zhu, P. Yuan, Y. Hu, G. Qu, B.-A. Lu, X. Xue, H. Yin, W. Cheng, J. Cheng, W. Xu, J. Li, J. Hu, S. Mu and J.-N. Zhang, *Nat. Commun.*, 2021, **12**, 1734.
29 J. Wang, H. Liu, J. Diao, X. Gu, H. Wang, J. Rong, B. Zong and D. S. Su, *J. Mater. Chem. A*, 2015, **3**, 2305–2313.
30 Y. Fang, D. Gu, Y. Zou, Z. Wu, F. Li, R. Che, Y. Deng, B. Tu and D. Zhao, *Angew. Chem., Int. Ed.*, 2010, **49**, 7987–7991.
31 Y. He, S. Hwang, D. A. Cullen, M. A. Uddin, L. Langhorst, B. Li, S. Karakalos, A. J. Kropf, E. C. Wegener, J. Sokolowski, M. Chen, D. Myers, D. Su, K. L. More, G. Wang, S. Litster and G. Wu, *Energy Environ. Sci.*, 2019, **12**, 250–260.
32 J. Woo, Y. J. Sa, J. H. Kim, H.-W. Lee, C. Pak and S. H. Joo, *ChemElectroChem*, 2018, **5**, 1928–1936.
33 X. Fu, N. Li, B. Ren, G. Jiang, Y. Liu, F. M. Hassan, D. Su, J. Zhu, L. Yang, Z. Bai, Z. P. Cano, A. Yu and Z. Chen, *Adv. Energy Mater.*, 2019, **9**, 1803737.
34 L.-S. Zhang, X.-Q. Liang, W.-G. Song and Z.-Y. Wu, *Phys. Chem. Chem. Phys.*, 2010, **12**, 12055–12059.
35 K. G. Latham, W. M. Dose, J. A. Allen and S. W. Donne, *Carbon*, 2018, **128**, 179–190.
36 X. Wang, W. Chen, L. Zhang, T. Yao, W. Liu, Y. Lin, H. Ju, J. Dong, L. Zheng, W. Yan, X. Zheng, Z. Li, X. Wang, J. Yang, D. He, Y. Wang, Z. Deng, Y. Wu and Y. Li, *J. Am. Chem. Soc.*, 2017, **139**, 9419–9422.
37 G. R. S. Iyer and P. D. Maguire, *J. Mater. Chem.*, 2011, **21**, 16162–16169.
38 J. Yang, Z. Qiu, C. Zhao, W. Wei, W. Chen, Z. Li, Y. Qu, J. Dong, J. Luo, Z. Li and Y. Wu, *Angew. Chem., Int. Ed.*, 2018, **57**, 14095–14100.
39 L. Bai, C.-S. Hsu, D. T. L. Alexander, H. M. Chen and X. Hu, *J. Am. Chem. Soc.*, 2019, **141**, 14190–14199.
40 Z. Zhang, J. Sun, F. Wang and L. Dai, *Angew. Chem., Int. Ed.*, 2018, **57**, 9038–9043.
41 L. Tao, M. Qiao, R. Jin, Y. Li, Z. Xiao, Y. Wang, N. Zhang, C. Xie, Q. He, D. Jiang, G. Yu, Y. Li and S. Wang, *Angew. Chem., Int. Ed.*, 2019, **58**, 1019–1024.
42 J. Li, L. Jiao, E. Wegener, L. L. Richard, E. Liu, A. Zitolo, M. T. Sougrati, S. Mukerjee, Z. Zhao, Y. Huang, F. Yang, S. Zhong, H. Xu, A. J. Kropf, F. Jaouen, D. J. Myers and Q. Jia, *J. Am. Chem. Soc.*, 2020, **142**, 1417–1423.
43 M. Qiao, Y. Wang, Q. Wang, G. Hu, X. Mamat, S. Zhang and S. Wang, *Angew. Chem., Int. Ed.*, 2020, **59**, 2688–2694.
44 N. M. Bedford, H. Ramezani-Dakhel, J. M. Slocik, B. D. Briggs, Y. Ren, A. I. Frenkel, V. Petkov, H. Heinz, R. R. Naik and M. R. Knecht, *ACS Nano*, 2015, **9**, 5082–5092.
45 V. Petkov, *Mater. Today*, 2008, **11**, 28–38.
46 K. W. Chapman, P. J. Chupas and C. J. Kepert, *J. Am. Chem. Soc.*, 2005, **127**, 11232–11233.
47 X. Xie, C. He, B. Li, Y. He, D. A. Cullen, E. C. Wegener, A. J. Kropf, U. Martinez, Y. Cheng, M. H. Engelhard, M. E. Bowden, M. Song, T. Lemmon, X. S. Li, Z. Nie, J. Liu, D. J. Myers, P. Zelenay, G. Wang, G. Wu, V. Ramani and Y. Shao, *Nat. Catal.*, 2020, **3**, 1044–1054.
48 I. S. Amiinu, X. Liu, Z. Pu, W. Li, Q. Li, J. Zhang, H. Tang, H. Zhang and S. Mu, *Adv. Funct. Mater.*, 2018, **28**, 1704638.
49 Z. Shi and J. Zhang, *J. Phys. Chem. C*, 2007, **111**, 7084–7090.
50 Y. Chen, S. Ji, S. Zhao, W. Chen, J. Dong, W.-C. Cheong, R. Shen, X. Wen, L. Zheng, A. I. Rykov, S. Cai, H. Tang, Z. Zhuang, C. Chen, Q. Peng, D. Wang and Y. Li, *Nat. Commun.*, 2018, **9**, 5422.
51 J. K. Nørskov, J. Rossmeisl, A. Logadottir, L. Lindqvist, J. R. Kitchin, T. Bligaard and H. Jónsson, *J. Phys. Chem. B*, 2004, **108**, 17886–17892.
52 C. J. Cramer, W. B. Tolman, K. H. Theopold and A. L. Rheingold, *Proc. Natl. Acad. Sci. U. S. A.*, 2003, **100**, 3635.
53 J.-X. Zhang, F. K. Sheong and Z. Lin, *Chem. - Eur. J.*, 2018, **24**, 9639–9650.